Appl Phys A (2009) 95: 125–130
DOI 10.1007/s00339-008-5035-8

Applied Physics A
Materials Science & Processing

Surface potential images of polycrystalline organic semiconductors obtained by Kelvin probe force microscopy

Haichao Huang · Haibo Wang · Jidong Zhang · Donghang Yan

Received: 2 September 2008 / Accepted: 24 November 2008 / Published online: 23 December 2008

Abstract *P*-type copper phthalocyanine (CuPc) and *n*-type hexadecafluorophthalocyanina-tocopper (F_{16}CuPc) polycrystalline films were investigated by Kelvin probe force microscopy (KPFM). Topographic and corresponding surface potential images are obtained simultaneously. Surface potential images are related with the local work function of crystalline facets and potential barriers at the grain boundaries (GBs) in organic semiconductors. Based on the spatial distribution of surface potential at GBs, donor- and acceptor-like trapping states in the grain boundaries (GBs) of *p*-CuPc and *n*-F_{16}CuPc films are confirmed respectively. In view of spatial energy spectrum in micro-scale provided by KPFM, it is going to be a powerful tool to characterize the local electronic properties of organic semiconductors.

PACS 07.79-.v · 68.35.-p · 73.61.Ph

1 Introduction

Electronic defects originated from grain boundaries (GBs) generally have considerable impact on energy levels for charge transport [1–3]. GB model was successfully applied to explain mobility increasing with grain size in *p*-type sexithiophene (6T) and octithiophene [1], and it was employed to interpret charge mobility dependence on dopant-concentration and gate voltage in *p*-type pentacene organic thin-film transistors (OTFTs) [2]. Conventional methods, such as current–voltage temperature-dependence and Hall measurements of thin-film devices, usually give the average results over all grains with different sizes and orientations. In order to further understand the relation between structures and electrical properties of GBs, it is necessary to get a microscopic view [4, 5]. Experimental inspections on *p*-6T GBs was done by using conducting AFM [3]. Unfortunately, it is hard to determine the type of traps by current–voltage measurements. Experimental observation of the type of trapping states, i.e., acceptor- or donor-like traps at GBs, is still an interesting problem.

KPFM [6] has proved to be a versatile tool for studying device physics and interface electronic structures of organic electronic devices [7]. For example, potential mapping on OTFTs [8–16], band bending at organic–metal interfaces [17–20], electrical and electronic properties of molecular thin films [7, 21–26], and surface photovoltaic effects under illumination in organic solar cells [27–31]. KPFM was also successfully applied to investigate GBs electrical properties in inorganic semiconductors, especially in $CuIn_xGa_{(1-x)}Se_2$ solar cells [32–34], but results of GBs in organic semiconductors are rarely reported [5]. KPFM records electrical potentials of sample surfaces, i.e., surface potentials. Different physical natures may contribute to the surface potential, such as surface dipole, charge density distribution, and energy band bending. The surface potential images provide electronic structure information of various surfaces and interfaces. Here we apply the KPFM to investigate the local work function and potential distribution around GBs in polycrystalline CuPc and F_{16}CuPc films.

H. Huang · H. Wang · J. Zhang · D. Yan (✉)
State Key Laboratory of Polymer Physics and Chemistry, Changchun Institute of Applied Chemistry, Graduate School of Chinese Academy of Sciences, Chinese Academy of Sciences, Changchun 130022, People's Republic of China
e-mail: yandh@ciac.jl.cn
Fax: +86-431-85262266

2 Experiments

To study the microscopic electrical properties of GBs, the proper morphology is necessary. Here we applied different substrates, i.e., highly oriented pyrolytic graphite (HOPG) and Polycrystalline Au films, and tuned the substrate temperature and deposit velocity to control the GBs morphology.

Gold was deposited onto precleaned Si slices as the conductive substrates. CuPc sample (Aldrich Chemical) was purified three times by gradient sublimation and then deposited to the polycrystalline Au substrates and freshly cleaved HOPG substrate at 2 nm/min by vacuum deposition under the pressure of 10^{-4} Pa. During deposition, the substrate temperature was held at 390 K. The total thickness of CuPc film is about 120 nm. Thus, we get the polycrystalline CuPc film. Preparation of F_{16}CuPc film on polycrystalline Au substrate is the same as above. We focus on the bulk properties of CuPc and F_{16}CuPc, so all the sample is thick enough to eliminate the possible interface influences, such as interface dipole [17].

The KPFM measurements were carried out on a commercial instrument (SPI3800N+SPA300HV, Seiko Instructions Inc., Japan) in air. Au-coated rectangle Si probe with spring constant of 2.8 N m^{-1} and resonant frequency of 28.9 kHz was used. The side parts of conductive substrates were electrically connected to KPFM system via silver paint. Topographical and surface potential images were recorded in dual-channel simultaneous dynamic force mode (DFM), i.e., in addition to the conventional DFM locked in resonant frequency for topography, a nonresonant alternating electronic signal $V_{ac}(\omega)$ with frequency of 26 kHz was applied to the cantilever in the second feedback loop to measure the surface potential simultaneously. In the KPFM, when probe keep proximal to the sample surface, the cantilever senses electrostatic force F_ω [7],

$$F_\omega = -\frac{\partial C}{\partial z}(V_{off} - V_{CPD})V_{ac}\sin(\omega t) \quad (1)$$

and vibrates at frequency of ω. When the feedback is closed, surface potential V_{CPD} is compensated by outer offset voltage V_{off}, and the electrostatic force F_ω between tip and sample is counteracted. In our measurements, surface potential value is independent of V_{ac} at the range of 1–15 V. The V_{ac} was set at 5–10 V when KPFM images were recorded. All the other scanning parameters were also optimized for good reproducibility.

3 Results and discussion

3.1 Local work function and contrast mechanism of KPFM

In KPFM application, the interpretation of contrast mechanism of surface potential images is not strictly defined due to different sample electrically conductive condition. Normally, the measurements can be divided into two types depending on whether the charge could flow (via electric circuitry of KPFM system) freely between sample surface and tip or not. When metals and semiconductors are measured by KPFM, electronic equilibrium can be achieved between sample and tip, so the surface potential can be interpreted in energy band landscape. For metals, the surface potential is the work function difference between the sample and tip [6, 35], and for most inorganic semiconductor, it related to surface band bending derived from Fermi energy level pinning due to surface defect states [36, 37]. However, for the samples of insulator or samples on insulator, the charge in samples cannot flow to tip, so the surface potential reflects real-space charge distribution in samples [38, 39].

As is known in the electronic equilibrium sample-tip system, potential signal of KPFM represents the Fermi energy level position of sample with respect to local vacuum level [40]. In our KPFM setup, the tip is electrically grounded, so the Fermi energy level equals the difference between tip's work function and surface potential,

$$\phi_s(x, y) = \phi_{tip} - eV_{CPD}(x, y) \quad (2)$$

$\phi_s(x, y)$ is the work function of sample related to lateral position, and ϕ_{tip} is the work function of tip. In KPFM, the measured VL is always relative to the VL of metallic tip. If we set the Fermi energy level as the reference level, which is constant throughout the sample and tip in electronic equilibrium, the contrast of surface potential image reveals the local vacuum level position, which varies with lateral position of sample surface [18, 38]. This is similar to the mechanism of work function measurement by ultraviolet photon spectroscopy [40, 41]. Here we use the polycrystalline CuPc to discuss the contrast mechanism of KPFM.

For the CuPc-HOPG sample, the growth process of CuPc on HOPG presents face-to-face packing mode in the surface normal direction [42], and the ordered molecular stacking is favorable to develop cryptographic facets with large grain size. Because of crystalline anisotropy of CuPc grains, different oriented facets are expected to have different work function, i.e., local work function. Figures 1a and b are the topology and surface potential images respectively, and Fig. 1c is the local work function image calculated from surface potential image (b) by formula (2). The work function of CuPc crystal varied form 4.87 eV to 5.02 eV depending on the orientations of facets. The surface potential image shows contrast upon different facets of grains. By chosen a line section in image (a) and (b), details are shown in image (d), the line (1) in the upper panel is the topography along the line in (a), and the line (2) in the lower panel is the surface potential along the line in (b). Facets A and B have an angle of ca. 43.5°, and that is also revealed by ca. 27 mV in their surface potential difference, which is larger

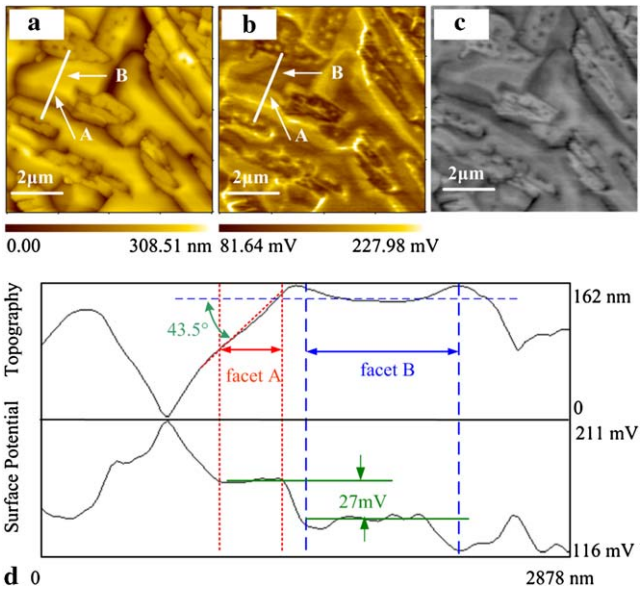

Fig. 1 CuPc polycrystalline films grown on HOPG. **a** Topographic image of CuPc. **b** Corresponding surface potential image. Scanning size is 8 μm × 8 μm. **c** Local work function image calculated from surface potential image **b**, z-range is 4.87–5.02 eV. **d** Line sections in **a** and **b**

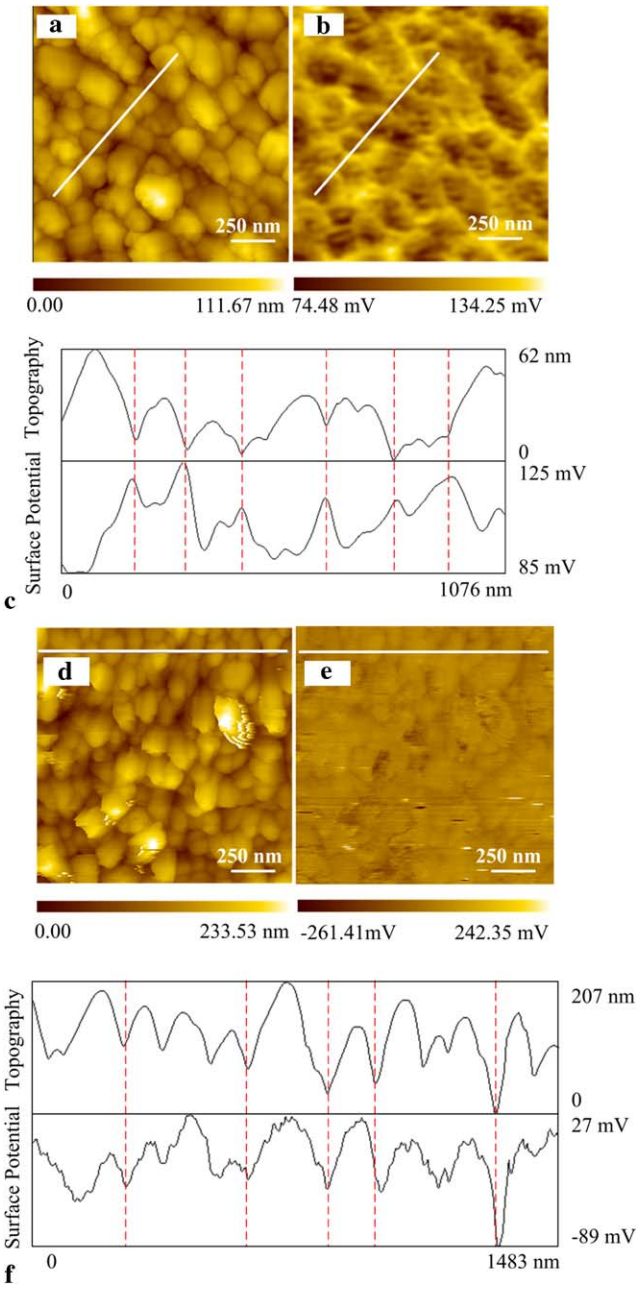

Fig. 2 CuPc and F_{16}CuPc polycrystalline films grown on polycrystalline Au substrates. **a** Topographic image of CuPc. **b** Corresponding surface potential image. Low pass FFT filter applied to slightly remove noise. Scanning size is 1.5 μm × 1.5 μm. **c** Line section in **a** and **b**. Dot lines give guide of GBs positions. **d**, **e**, **f** are topographic, surface potential, and line section images of polycrystalline F_{16}CuPc respectively. The AC voltage is 5–8 V, and scanning speed is 0.2–0.3 Hz

enough than our KPFM's nominal resolution of 3 mV. The results of CuPc are similar to previous reports of work functions dependence on the grain facets orientation in $CuGaSe_2$ demonstrated by KPFM [43].

Cahen and Kahn [40] have discussed the concepts of local work function and local vacuum level recently. In dual-channel simultaneous mode KPFM, the probe keeps within several tens nm to the surface. This distance is small enough compared to the surface dimension, which is several micrometers in Fig. 1a, so the tip-sensed electrostatic field mainly derives from the surface that is just under the tip. Thus, the KPFM measured work function is that of the surface, and the detected vacuum level is the *local* vacuum level of that surface [40]. The work function contrast of different surfaces may come from the different surface electronic structure of CuPc crystal facets. This reflects microscopic molecular packing and orientation impact on its local electronic structure [44].

3.2 Types of trap state from grain boundary defect

CuPc and F_{16}CuPc grown on polycrystalline Au substrates are consisted of small and irregular grains. Figure 2a shows the topographic image of CuPc. Grain size of CuPc varies from 50 to 300 nm. Figure 2b shows the corresponding surface potential image of CuPc. The GBs and their vicinity are brighter than the bulk region, which suggest a downward band bending of local vacuum level and valence band at GB. The local band bending of valence level and conduction level follows the local vacuum level. Thus, hole depletion space-charge region (SCR) are formed around GB. Figure 2c is the line section in (a) and (b); the surface potential shows a close track of its topography, and potential barriers are observed clearly at each GB. The barrier heights vary from 30 to 60 meV. For *p*-type CuPc, the GBs introduce donor-like trapping levels within the band gap. These

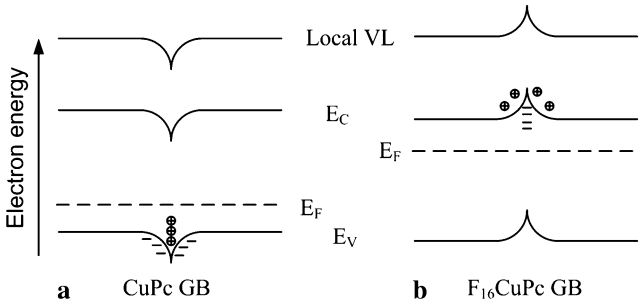

Fig. 3 Schematic energy level diagrams of CuPc **a** and F_{16}CuPc **b** GBs. Illustrated the positively and negatively charged GBs in CuPc and F_{16}CuPc, respectively. Local band bending occurred according to surface images in Fig. 2

trapping states are capable of trapping carriers and become positively charged and creating potential energy barriers at GBs. The GBs potential barriers also clearly appear in CuPc-HOPG sample (see Fig. 1).

Figure 2d–f shows the case for F_{16}CuPc. For *n*-type F_{16}CuPc, the local vacuum level and conduction band bends upwards at GBs. It suggests potential barriers for electron and acceptor-like trapping levels located in the F_{16}CuPc GBs. Figure 3 shows the schematic energy level diagrams of CuPc and F_{16}CuPc GBs.

The physical origin of GB defect states in organic semiconductors is not clear for now. In covalent bonded inorganic semiconductors, the interface broken bonds and disorder atoms create the GBs defect states and GB potential barrier usually modeled by back-to-back Schottky barrier [45]. However, in van der Waals bonded organic semiconductors, surface states lie outside the band gap [19, 22], and there seems no Fermi level pinning at the surface. Thus, the break of crystal potential at the GBs cannot lead to the form of potential barriers in organic semiconductors. Some other mechanisms maybe contribute to it. Previous theoretical study on pentacene GBs has pointed out that void, molecular disorder, crystallographic orientation misalign, and foreign molecular dwelling at GBs can form GB defect states [46].

3.3 The effect of grain size

Moreover, it is clearly shown that in the CuPc sample the barrier heights are dependent on the grain sizes. In Figs. 4a and b the large grains have flat ground in the interior and are decorated with barrier around. Figure 4a is the topographic image of a large grain with size of 252 nm. In the corresponding surface potential image, Fig. 4b, the line section demonstrates that surface potential is composed of a flat region of grain bulk and depleted region at each side of the GBs, the width of the depleted regions is ca. 92 nm, and the height of GB barrier potential is ca. 35 meV. For the small grains in Figs. 4c and d, the barrier heights are lower than

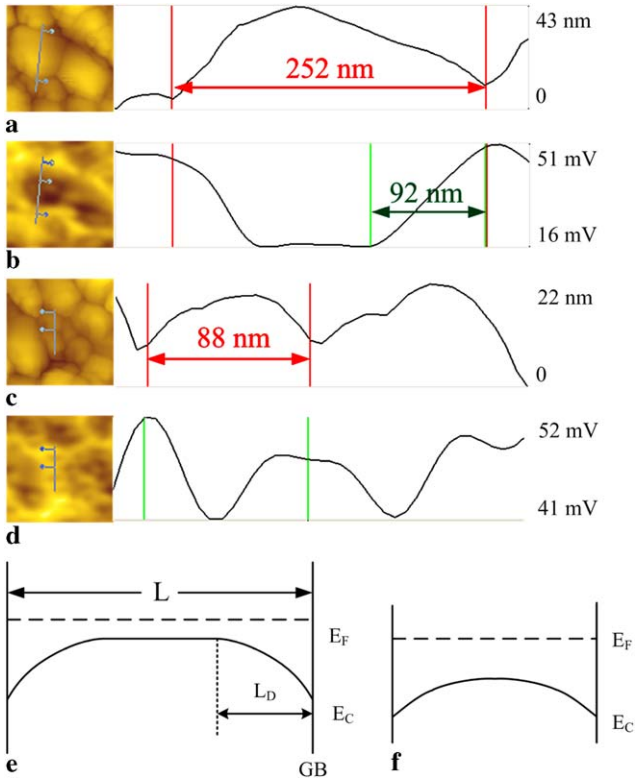

Fig. 4 CuPc GBs barriers vary with grain sizes. **a** and **b** topographic, surface potential image, and line sections of large grains. **c** and **d** topographic, surface potential image, and line sections of small grains. Schematic band diagrams of large grains **e** $L > 2L_D$ and of small grains **f** $L < 2L_D$

that of large GBs. From line sections of a small grain with size of 88 nm, it is clearly that the depletion regions extend completely through the grain, and the height of GB barrier potential has a lower value of ca. 11 meV. Though crystallographic orientation has contribution to the surface potential contrast, the potential barriers at GBs are more prominent than the surface potential variation that comes from crystallographic orientation. The grain size effect can be clearly determined.

Theoretical model of GBs was proposed in inorganic semiconductors [45, 47]. In the model, the barrier height is dependent on the carrier concentration N, trap density N_t, and grain size L as follows:

$$E_b = \frac{e^2 N_t^2}{8\varepsilon_s \varepsilon_0 N} \quad (L > 2L_D) \tag{3}$$

$$E_b = \frac{e^2 L^2 N}{8\varepsilon_s \varepsilon_0} \quad (L < 2L_D) \tag{4}$$

The distinction is the magnitude of Debye length L_D and grain size L. $L_D = \sqrt{\varepsilon_s \varepsilon_0 k_B T / e^2 N}$ is the characteristic length of space-charge region (SCR) and screen length against the trapped charges at the GBs. The L_D was also applied to explain charge accumulation thickness at organic

heterojunction interfaces [48]. For large grains, in Figs. 4a, b, and e, $L > 2L_D$, the traps are fully filled, and only part of the grain is depleted. The barrier height E_b only depends on trap states in the GBs. But for small grains, in Fig. 4c, d and f, $L < 2L_D$, the traps are partially filled, and the E_b increases with grain size. From the surface potential images of CuPc, we can determine that L_D is about 100 nm, and this coincides with the calculated value about 200 nm, assuming that the ε_s of CuPc is 1.6 [49] and that the carrier concentration is 10^{14} cm^{-3} [50]. The grain size effect implies that carrier transport in polycrystalline organic semiconductors is GBs-limited. The height and width of GB potential barriers determine the probability of electron thermoemit and tunneling through the GBs, respectively. The revealed grain size effect is in accordance with grain size dependence of charge transport mobility in OTFTs [1].

In long-distance electrostatic interaction, the tip-sample distance has great influence on the lateral resolution [7]. The effective capacitance is not only limited to tip apex but strongly depends on the sidewall area of tip. When the tip-sample distance is small (several tens nm), the capacitance is determined mostly by the tip apex and the area just under it. However, when the distance is larger (several hundreds nm), the sidewall of tip comes into the main influence, and the broaden effect appears in surface potential image [20, 24, 51]. In the dual-channel simultaneous mode, the tip-sample distance is just as that of dynamic force microscopy, and the broadening effect at GBs can be safely neglected [24]. The GBs potential barriers in surface images really demonstrate the size correlation effect.

4 Conclusion

In conclusion, KPFM was applied to characterize the local work function GBs in organic semiconductors. The local work function reflects that molecular orientation has impact on electronic structure in organic semiconductor. Surface potential images are interpreted as local band bending. Potential barriers and trapping states appeared at GBs in *p*-CuPc and *n*-F_{16}CuPc crystalline films were observed. Donor-like trapping states are present at GBs in *p*-type CuPc, and acceptor-like trapping states are present at GBs in *n*-type F_{16}CuPc. The effect of potential barriers depending on grain sizes was also observed. KPFM is demonstrated to be a powerful tool to characterize the relations between local structures and electronic properties in organic semiconductors at nanoscale.

Acknowledgements This work was supported by the National Natural Science Foundation of China (50773079, 20621401).

References

1. G. Horowitz, M.E. Hajlaoui, Adv. Mater. **12**, 1046 (2000)
2. S. Verlaak, V. Arkhipov, P. Heremans, Appl. Phys. Lett. **82**, 745 (2003)
3. A.B. Chwang, C.D. Frisbie, J. Appl. Phys. **90**, 1342 (2001)
4. T.W. Kelley, C.D. Frisbie, J. Phys. Chem. B **105**, 4538 (2001)
5. K. Puntambekar, J.P. Dong, G. Haugstad, C.D. Frisbie, Adv. Funct. Mater. **16**, 879 (2006)
6. M. Nonnenmacher, M.P. O'Boyle, H.K. Wickramasinghe, Appl. Phys. Lett. **58**, 2921 (1991)
7. V. Palermo, M. Palma, P. Samor, Adv. Mater. **18**, 145 (2006)
8. L. Burgi, H. Sirringhaus, R.H. Friend, Appl. Phys. Lett. **80**, 2913 (2002)
9. L. Burgi, T.J. Richards, R.H. Friend, H. Sirringhaus, J. Appl. Phys. **94**, 6129 (2003)
10. L. Burgi, T. Richards, M. Chiesa, R.H. Friend, H. Sirringhaus, Synth. Met. **146**, 297 (2004)
11. K.P. Puntambekar, P.V. Pesavento, C.D. Frisbie, Appl. Phys. Lett. **83**, 5539 (2003)
12. S. Ikeda, T. Shimada, M. Kiguchi, K. Saiki, J. Appl. Phys. **101** (2007)
13. O. Tal, Y. Rosenwaks, Y. Preezant, N. Tessler, C.K. Chan, A. Kahn, Phys. Rev. Lett. **95** (2005)
14. O. Tal, Y. Rosenwaks, Y. Roichman, Y. Preezant, N. Tessler, C.K. Chan, A. Kahn, Appl. Phys. Lett. **88** (2006)
15. S.G.J. Mathijssen, M. Colle, A.J.G. Mank, M. Kemerink, P.A. Bobbert, D.M. de Leeuw, Appl. Phys. Lett. **90** (2007)
16. E.C.P. Smits, S.G.J. Mathijssen, M. Colle, A.J.G. Mank, P.A. Bobbert, P.W.M. Blom, B. de Boer, D.M. de Leeuw, Phys. Rev. B **76**, 125202 (2007)
17. H. Ishii, N. Hayashi, E. Ito, Y. Washizu, K. Sugi, Y. Kimura, M. Niwano, Y. Ouchi, K. Seki, Phys. Status Solidi (a) **201**, 1075 (2004)
18. L.W. Chen, R. Ludeke, X.D. Cui, A.G. Schrott, C.R. Kagan, L.E. Brus, J. Phys. Chem. B **109**, 1834 (2005)
19. D. Cahen, A. Kahn, E. Umbach, Mater. Today **8**, 32 (2005)
20. J. Colchero, A. Gil, A.M. Baro, Phys. Rev. B **64**, 245203 (2001)
21. M. Fujihira, Annu. Rev. Mater. Sci. **29**, 353 (1999)
22. M. Pfeiffer, K. Leo, N. Karl, J. Appl. Phys. **80**, 6880 (1996)
23. V. Palermo, M. Palma, Z. Tomovic, M.D. Watson, R. Friedlein, K. Mullen, P. Samori, Chem. Phys. Chem. **6**, 2371 (2005)
24. A. Liscio, V. Palermo, D. Gentilini, F. Nolde, K. Mullen, P. Samori, Adv. Funct. Mater. **16**, 1407 (2006)
25. V. Palermo, S. Morelli, M. Palma, C. Simpson, F. Nolde, A. Herrmann, K. Mullen, P. Samori, Chem. Phys. Chem. **7**, 847 (2006)
26. A. Liscio, V. Palermo, P. Samorì, Adv. Funct. Mater. **18**, 907 (2008)
27. H. Hoppe, T. Glatzel, M. Niggemann, A. Hinsch, M.C. Lux-Steiner, N.S. Sariciftci, Nano Lett. **5**, 269 (2005)
28. H. Hoppe, T. Glatzel, M. Niggemann, W. Schwinger, F. Schaeffler, A. Hinsch, M.C. Lux-Steiner, N.S. Sariciftci, Thin Solid Films **511–512**, 587 (2006)
29. D.C. Coffey, D.S. Ginger, Nat. Mater. **5**, 735 (2006)
30. A. Liscio, G. DeLuca, F. Nolde, V. Palermo, K. Mullen, P. Samori, J. Am. Chem. Soc. (2007)
31. V. Palermo, G. Ridolfi, A.M. Talarico, L. Favaretto, G. Barbarella, N. Camaioni, P. Samori, Adv. Funct. Mater. **17**, 472 (2007)
32. S. Siebentritt, S. Sadewasser, M. Wimmer, C. Leendertz, T. Eisenbarth, M.C. Lux-Steiner, Phys. Rev. Lett. **97**, 146601 (2006)
33. T. Glatzel, D.F. Marron, T. Schedel-Niedrig, S. Sadewasser, M.C. Lux-Steiner, Appl. Phys. Lett. **81**, 2017 (2002)
34. C.S. Jiang, F.S. Hasoon, H.R. Moutinho, H.A. Al-Thani, M.J. Romero, M.M. Al-Jassim, Appl. Phys. Lett. **82**, 127 (2003)
35. M.P. O'Boyle, T.T. Hwang, H.K. Wickramasinghe, Appl. Phys. Lett. **74**, 2641 (1999)

36. S. Hudlet, M.S. Jean, B. Roulet, J. Berger, C. Guthmann, J. Appl. Phys. **77**, 3308 (1995)
37. Y. Rosenwaks, R. Shikler, T. Glatzel, S. Sadewasser, Phys. Rev. B **70**, 085320 (2004)
38. S.V. Kalinin, D.A. Bonnell, Phys. Rev. B **62**, 10419 (2000)
39. Y. Shen, D.M. Barnett, P.M. Pinsky, Rev. Sci. Instrum. **79**, 023711 (2008)
40. D. Cahen, A. Kahn, Adv. Mater. **15**, 271 (2003)
41. N.K.W.G. Antoine Kahn, J. Polym. Sci., Part B: Polym. Phys. **41**, 2529 (2003)
42. S.D. Wang, X. Dong, C.S. Lee, S.T. Lee, J. Phys. Chem. B **108**, 1529 (2004)
43. S. Sadewasser, T. Glatzel, M. Rusu, A. Jager-Waldau, M.C. Lux-Steiner, Appl. Phys. Lett. **80**, 2979 (2002)
44. S. Duhm, G. Heimel, I. Salzmann, H. Glowatzki, R.L. Johnson, A. Vollmer, J.P. Rabe, N. Koch, Nat. Mater. **7**, 326 (2008)
45. J.Y.W. Seto, J. Appl. Phys. **46**, 5247 (1975)
46. S. Verlaak, P. Heremans, Phys. Rev. B **75**, 115127 (2007)
47. J.W. Orton, M.J. Powell, Rep. Prog. Phys. **43**, 1263 (1980)
48. Y. Gao, H. Ding, H. Wang, D. Yan, Appl. Phys. Lett. **91**, 142112 (2007)
49. H. Vázquez, F. Flores, A. Kahn, Org. Electron. **8** (2007)
50. G. Horowitz, Adv. Funct. Mater. **13**, 53 (2003)
51. E. Strassburg, A. Boag, Y. Rosenwaks, Rev. Sci. Instrum. **76**, 083705 (2005)